Lab on a Chip

Microneedle-Integrated Distance-Based Paper Device for Simultaneous Transdermal Detection of Cortisol and Dopamine

Journal:	*Lab on a Chip*
Manuscript ID	LC-ART-11-2024-000983.R2
Article Type:	Paper
Date Submitted by the Author:	24-Mar-2025
Complete List of Authors:	dos Santos, Danilo; Tufts University, Department of Electrical and Computer Engineering; Tufts University, Sonkusale Research Labs Khachornsakkul, Kawin; Tufts University, Department of Electrical and Computer Engineering; Sonkusale Research Labs, Department of Electrical and Computer Engineering Sonkusale, Sameer; Tufts University, Department of Electrical and Computer Engineering; Sonkusale Research Labs, Department of Electrical and Computer Engineering

Microneedle-Integrated Distance-Based Paper Device for Simultaneous Transdermal Detection of Cortisol and Dopamine

Danilo Martins dos Santos[a,b+], Kawin Khachornsakkul[a,b+], Sameer Sonkusale[a,b*]

[a]Department of Electrical and Computer Engineering, Tufts University, Medford, MA 02155, USA

[b]Sonkusale Research Labs, Halligan Hall, Tufts University, Medford, MA 02155, USA

+ Shared first author

Corresponding author: sameer.sonkusale@tufts.edu

Abstract

Accurate measurement of stress marker cortisol and neurotransmitter dopamine is essential for understanding the physiological effects of chronic stress, enabling early therapeutic interventions to prevent adverse health consequences. Herein, we introduce the first fully integrated wearable device comprising a microneedle (MN) patch and distance-based paper analytical device (dPAD) for minimally invasive dermal interstitial fluid (ISF) sampling and simultaneous cortisol and dopamine sensing. The MN patch employs a swellable hydrogel matrix for efficient ISF extraction, whereas the simple dPAD sensor can simultaneously detect cortisol and dopamine through colorimetric reactions. Quantitative analysis was achieved through simple measurement of the colored distance proportional to the analyte concentration using a ruler. The device demonstrates high sensitivity, with detection limits of 0.25 μg mL^{-1} for cortisol and 1.0 ng mL^{-1} for dopamine, along with excellent selectivity for both analytes. It also exhibited high accuracy and precision, with recovery rates of 98.5–100.7% for cortisol and 98.8–102.2% for dopamine. These results show that the developed sensor device is user-friendly, simplifies the analysis process, reduces costs, and eliminates the need for complex instrumentation, making it a promising tool for point-of-care (POC) testing for stress and its relative disorders, with potential applications in diagnosing other biomarkers.

Keywords: Microneedles, distance-based paper analytical devices (dPADs), wearable sensor, point-of-care (POC) testing, stress biomarkers

1 Introduction

Chronic stress is characterized by the abnormal secretion of cortisol and dopamine, which can significantly affect both physical and mental health[1]. Cortisol, the primary hormone associated with stress, typically exhibits a diurnal rhythm, peaking in the morning and decreasing throughout the day[2]. However, chronic stress can disrupt this pattern, resulting in persistently elevated or erratic fluctuations in cortisol levels, which may contribute to conditions such as hypertension, immune dysfunction, and metabolic disorders[1,2]. Similarly, dopamine, an essential neurotransmitter involved in mood regulation and reward pathways, can exhibit dysregulated secretion under chronic stress, potentially leading to mood disorders including depression, anxiety, and cognitive impairments[3]. Therefore, it is crucial to monitor cortisol and dopamine levels for timely diagnosis and prognosis clinically to rapid treatment, thereby reducing the adverse effects of chronic stress on health.

In recent years, various methods have been developed for the detection of cortisol and dopamine, including high-performance liquid chromatography[4,5], surface-enhanced Raman spectroscopy (SERS)[6,7], and electrochemical methods[8]. However, these methods are complex, time-consuming, and expensive, requiring extensive sample preparation and skilled personnel. [9]. The development of various sensors for stress biomarkers, including wearables, has shown promise[10]. Among the body fluids used for the detection of stress hormones, sweat-based sensing, which uses non-invasive on-skin methods, is appealing but challenging because of the difficulty in collecting sufficient sweat for accurate measurements [11]. Salivary detection involves collecting saliva through spits or swabs, posing challenges in continuous monitoring and accuracy[10]. Blood, the clinical standard, exhibits higher stress hormone concentrations compared to sweat and saliva, but it can be painful and stressful for patients[12,13].

Transdermal biosensing is an innovative approach for continuous, noninvasive, or minimally invasive monitoring of a patient's health by analyzing interstitial fluid (ISF), which is the fluid present in the dermis, the lower layer of the skin [14,15]. ISF offers a unique advantage as a sample for biomarker detection due to its close molecular composition to blood plasma and the presence of relevant biomarkers[14]. ISF can be sampled conveniently using microneedle (MN) technology in a pain-free, minimally invasive, and

user-friendly manner [16,17]. Several MN designs are available, each of which employs distinct strategies for ISF acquisition[18]. Among them, hydrogel-based MNs (HMNs) represent the latest advancements by leveraging the inherent absorption properties of the material [19,20]. Compared with other MN types, HMNs offer several advantages, including increased and faster ISF extraction, high biocompatibility, lower fabrication costs, higher production yields, and ease of insertion and removal with minimal to no skin damage[21–24].

Microneedles (MNs) integrated with biosensors enable real-time characterization of interstitial fluid (ISF) [18,25–27]. However, integrating recognizing elements, such as enzymes and dyes, into MNs raises concerns about reagent leakage and skin irritation[28–30]. Additionally, these sensing platforms often rely on complex instrumentation for signal readout, which limits their use in resource-limited settings. Distance-based paper analytical devices (dPADs) offer several advantages for compact and efficient sample-to-answer readouts [31]. These advantages include the use of environmentally sustainable and biodegradable paper substrates, low-cost operation, minimal reagent or sample consumption, and no requirement for sample preparation. Colorimetric dPADs, in particular, allow on-site monitoring without the need for software or instrumentation, providing both ease of use and affordability[32,33]. In these devices, the sample solution flows into the hydrophilic channels of the paper platform through capillary action where it reacts with pre-deposited reagents, resulting in a color change proportional to the analyte concentration[34]. This color change can be quantified by measuring the length of the color change along the channel, allowing for a naked-eye readout using a ruler[35]. Although paper-based devices integrated with hydrogel microneedles have been previously described for transdermal biomarker detection [28], the integration of dPADs and microneedle devices for sample acquisition and multi-analyte quantification in a single device has not been reported.

Here, we introduce a fully integrated microneedle-distance-based paper analytical device (MNs-dPAD) for simultaneous transdermal detection of cortisol and dopamine, as illustrated in Figure 1. The straightforward dPAD was designed to consist of a sample zone in contact with the hydrogel microneedles, and two straight detection zones where the reaction occurs. Cortisol sensing is achieved by monitoring the formation of a nitro

blue formazan by reacting with blue tetrazolium and a tetramethylammonium hydroxide (TMAOH). Meanwhile, the reduction reaction of cerium (IV) ions (Ce^{4+}) induced color change is used for quantification of dopamine levels in the ISF. The hydrogel MNs, fabricated from a biocompatible poly(acrylic acid) (PAA)/gelatin methacrylate (GelMA) matrix, exhibit high swelling capacity and robust mechanical properties [36,37]. Upon collection of ISF sample by the MNs, the ISF promptly migrates to the sample zone of the paper channel. The target biomolecules interact with their specific pre-deposited reagents along the length of the detection channel, resulting in color change as a function of distance. Subsequently, a ruler is utilized for visual quantification of cortisol and dopamine, respectively, in each channel. Given the facile fabrication and cost-effective monitoring of both cortisol and dopamine levels in ISF, in a wearable format, MNs-dPAD has the potential to improve the diagnosis and management of chronic stress. Furthermore, this device can be used and operated by an unskilled user at home or in a community health setting. The device can also be expanded by adding more detection channels to detect other relevant biomarkers in the future.

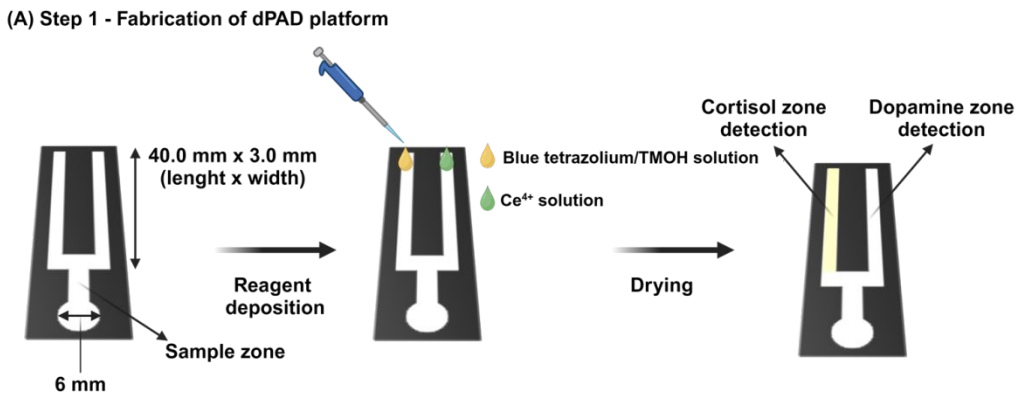
(A) Step 1 - Fabrication of dPAD platform
40.0 mm x 3.0 mm
(lenght x width)
6 mm
Sample zone
Reagent
deposition
Blue tetrazolium/TMOH solution
Ce4+ solution
Drying
Cortisol zone
detection
Dopamine zone
detection

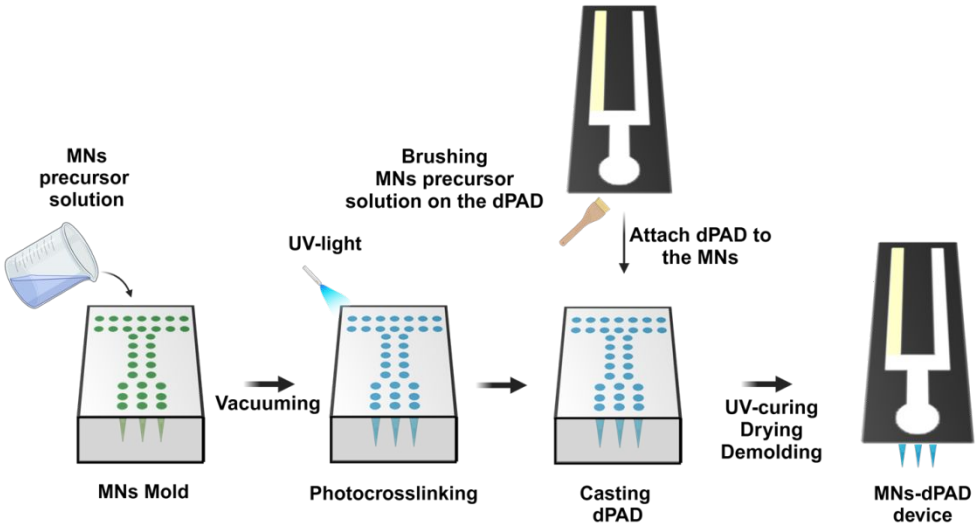
(B) Step 2 - Integration of MNs in the d-PAD platform
MNs
precursor
solution
MNs Mold
Vacuuming
UV-light
Photocrosslinking
Brushing
MNs precursor
solution on the dPAD
Attach dPAD to
the MNs
Casting
dPAD
UV-curing
Drying
Demolding
MNs-dPAD
device

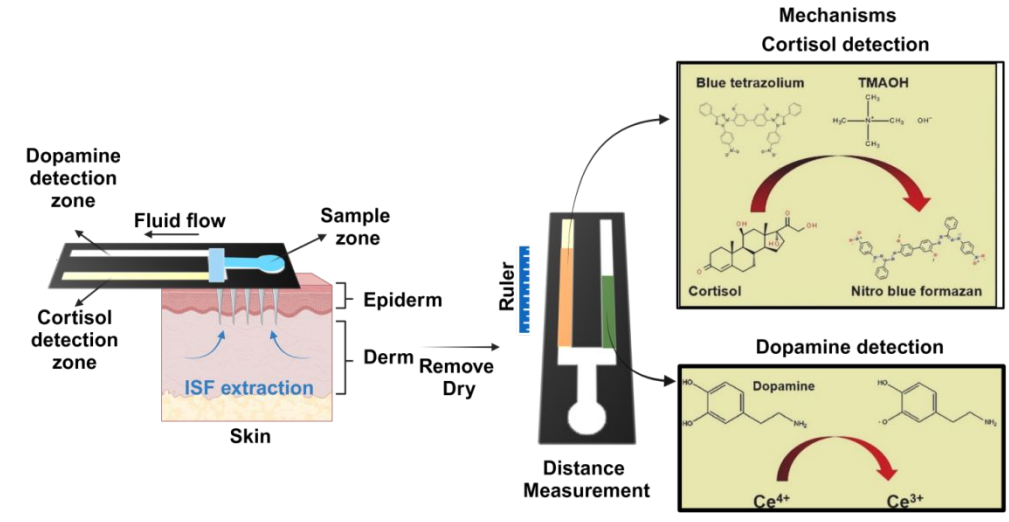
(C) Step 3 - Transdermal quantification of cortisol and dopamine using the MNs-dPAD device
Dopamine
detection
zone
Fluid flow
Sample
zone
Cortisol
detection
zone
Epiderm
Derm
ISF extraction
Skin
Remove
Dry
Ruler
Distance
Measurement
Mechanisms
Cortisol detection
Blue tetrazolium
TMAOH
Cortisol
Nitro blue formazan
Dopamine detection
Dopamine
Ce4+
Ce3+

Figure 1. Schematic illustration of fabrication and detection mechanism of MNs-dPAD. (A) A wax printer was used to fabricate the dPAD with a sample zone and two detection zones. The detection zones were functionalized with tetramethylammonium hydroxide (TMAOH)/blue tetrazolium and Ce^{4+} solutions to detect cortisol and dopamine, respectively. (B) Integration of PAA/GelMA MNs into the dPAD platform. MNs were fabricated using a micromolding technique and subsequently integrated into the sample zone of the dPAD. (C) Schematic representation of detection mechanism. Upon sample collection, target analytes (cortisol and dopamine) diffuse into the MNs and react with the immobilized reagents in the detection zones, generating a colorimetric response.

2. Experimental section

2.1. Materials

Type A gelatin from porcine skin (300 bloom), methacrylic anhydride (MA, 94%), poly (acrylic acid) (PAA, Mw=100,000, 35 wt. % in H_2O), lithium phenyl-2,4,6-trimethylbenzoylphosphinate (LAP, photoinitiator), tetramethylammonium hydroxide (TMAOH), blue tetrazolium, and other chemicals were purchased from Sigma-Aldrich. Whatman No.1 filter paper was obtained from Growing Labs (USA). GelMA was synthesized according to a method previously reported in the literature [38]. Its characterization was performed using proton nuclear magnetic resonance (^{1}H NMR) spectroscopy, and the average degree of substitution (DS) was calculated based on a methodology reported in literature[38], resulting in a DS value of 59.2%. Porcine ear skin was obtained from a local supermarket.

2.2. Fabrication of MNs-dPADs

The fabrication of the proposed MNs-dPAD for simultaneous detection of cortisol and dopamine is illustrated in Figure 1. Briefly, the dPAD was first designed with a one sample zone and two straight detection zones (3.0 x 40.0; width x length) by using the Adobe Illustrator software. Afterwards, the designed paper was printed using a wax printer (Xerox ColorQube, Japan) and subsequently melted at 120 °C for 2 min. The backside of the braked paper was taped with adhesive tape to prevent solution leakage through the device. Thereafter, a solution of blue tetrazolium and TMAOH was deposited

into the left-side detection zone, whereas the Ce^{4+} solution was coated into the right-side detection zone. The device was then dried at room temperature.

MNs were fabricated using a micromolding technique (Figure 1B)[39]. GelMA was dissolved in water at 60 °C for 1 hour, cooled to 40 °C, and then mixed with PAA/LAP (photoinitiator, PI) for 30 min. at 40 °C. The final GelMA and PI concentrations were 50 and 5 mg/g, respectively. To evaluate the impact of PAA concentration on MN formation, three levels (75, 125, and 250 mg/g) were tested. A 0.95 mL aliquot of the precursor solution was dispensed into a 42-MN array mold, with each microneedle measuring 1,200 μm in height and 1,000 μm in base radius, distributed over a 1.2 cm^2 area corresponding to the sample zone. Notably, microneedles were positioned exclusively beneath the sample zone. The mold was fabricated from Ecoflex™ 00-50 silicone (Smooth-On, Inc., Macungie, PA, USA) using a cost-effective and versatile cross-over-lines (COL) method, as detailed in our previous study[39]. To eliminate air bubbles, the filled mold underwent vacuum treatment at 500 mmHg and 40 °C. Subsequently, the mold was exposed to a 70 W UV light source at 405 nm (Form Cure, Formlabs, Cambridge, MA, USA) for 5 min. to initiate crosslinking and solidify the solution within the tip cavities. After 12 h of drying at 25 °C, 0.15 mL the MN precursor solution was applied to the sample zone of the dPAD platform. Subsequently, the MNs-dPAD patch was dried at 25 °C for 12 hours, removed from the mold via stretching, and UV-irradiated for an additional 5 min. through the needle side to complete the crosslinking process. The morphology of the EU-MNs was characterized by using optical microscopy (Keyence VHX-7000 series, IL, USA) and scanning electron microscopy (SEM, ThermoFisher Axia ChemiSEM, MA, USA). SEM imaging was conducted at an acceleration voltage of 10 kV, following gold sputter coating (MicroNano Tools MNT-JS1600 system, BC, CAN).

2.3. MNs-dPAD characterization

2.3.1. General optimization and analytical procedure

To optimize the efficiency of the dPAD, 30.0 μL of the standard solution containing cortisol (6.0 μg mL^{-1}) and dopamine (15.0 ng mL^{-1}) were added to the sample zone of the device and allowed to equilibrate at room temperature for 10 min. The colored distances in both detection zones were subsequently measured using a conventional ruler with a

resolution of 1.0 mm. All experiments were conducted in triplicate (n = 3). Linear ranges of the dPAD for cortisol and dopamine quantification were established by introducing a solution containing cortisol and dopamine at varying concentrations. Detection was performed as previously described (n = 3). The limit of detection (LODs) was determined by measuring the lowest concentrations of the analytes that could generate the minimum distance signals in the device. The reproducibility of the method was evaluated by detecting both analytes ten times (n = 10) and subsequently calculating the relative standard deviation (RSD) to validate the precision. Furthermore, assay selectivity was assessed by measuring the distance signal of other substrates compared to that of the analytes alone. Similarly, the interferences were examined by monitoring the distance signals of the mixed solution between the analytes and other substrates, compared to that of the analyte alone (n = 3). For biomedical analysis, artificial interstitial fluids were spiked with a standard solution and introduced into the sample zone of the device. The detection procedures were performed as described previously, and the recovery percentage was calculated (n = 3).

2.3.1. Mechanical Test and Skin Penetration Efficiency

Porcine skin was obtained from a local market, cleaned with deionized water, shaved, and trimmed using a scalpel. A PAA/GelMA MNs-dPAD was applied to a 2 × 2 cm area of the skin for 5 min using thumb pressure. Subsequently, a 1 × 1 cm skin section was excised, embedded in a resin block, frozen at -80 °C, sectioned into 10-μm thick slices, and stained with hematoxylin and eosin (H&E) (Abcam, USA). Penetration hole morphologies were imaged and captured using an optical microscope (Keyence, model VHX-7000 series, IL, USA). The mechanical strength of the MN patches was evaluated using a universal testing machine (INSTRON model 5900, MA, USA). Patches were positioned flat on their backside (tips upward) on a compression platen with a 1.5 mm gap to the opposing platen. Vertical force was applied at a constant speed of 0.5 mm/min. The compression loading cell capacity was set to 50 N. Load (force, N) and displacement (distance, mm) data were recorded every 0.1 s to generate load-displacement curves. At least five samples were tested for each type of specimen

2.3.2. Swelling Studies

The ISF extraction capacity of MNs-dPAD was evaluated using a gravimetric method in agarose and porcine skin models. A 1.4 wt% agarose hydrogel was prepared in 1x PBS and covered with parafilm. Porcine skin was equilibrated in 1x PBS overnight. The initial dry mass (W_0) of the MNs-dPAD was determined prior to application to either the agarose or porcine skin models. Following application, the MNs-dPAD was allowed to swell for specific time points (0, 2, 4, 6, 8, 10, 12, 14, 16, 18, and 20 min), and the mass (W_t) of the swollen patches was measured. The extracted ISF volume (V_{ISF}) was calculated using the following formula: $V_{isf} = (W_t – W_0)/\rho_{PBS}$, where ρ_{PBS} is the density of the PBS solution at 25°C (ρ_{PBS} = 1.01 g/mL). To quantify the ISF collection within the dPAD sample zone, microneedle PAA/GelMA MNs with a hydrophobic substrate were fabricated, and the V_{ISF} was compared with that of the original MNs-dPAD. Each experiment was replicated four times for each patch at the specified time points.

2.4 In Vitro and Ex Vivo Detection of Cortisol and Dopamine Using An Agarose Hydrogel And Porcine Skin Models

MNs-dPADs were applied to 1.4 wt% agarose hydrogels coated with parafilm mimicking a skin tissue and containing varying concentrations of cortisol (0.0, 2.0, 4.0, 6.0, and 8.0 μg mL^{-1}) and dopamine (0.0, 5.0, 10.0, 15.0, and 20.0 ng mL^{-1}). MNs-dPADs were also applied to porcine skin equilibrated overnight in 1× PBS containing the same concentrations of cortisol and dopamine mentioned above. In both agarose and porcine skin models, ISF collection was performed at 37 °C for 18 min. Following ISF extraction, MNs-dPADs were removed and 15 μL of 1x PBS was added to the sample zone. Colorimetric changes in both detection zones were measured after 10 min at room temperature, using a traditional ruler (resolution: 1.0 mm). All experiments were conducted in triplicate.

2.5. Statistical analysis

All data were presented as mean ± standard deviation. To assess statistically significant differences, a one-way analysis of variance (ANOVA) was conducted, followed by Tukey’s post hoc test at a 95% confidence level, using Origin software version 2019b (OriginLab Corporation, Northampton, MA, USA).

3. Results and discussion

3.1. MNs-dPADs fabrication and characterization

In this study, we introduce a wearable device comprising a microneedle (MN) platform integrated into a distance-based paper analytical device (dPAD) for the colorimetric transdermal detection of cortisol and dopamine. MNs were fabricated using a straightforward micromolding technique with a PAA /GelMA matrix and then integrated to the dPAD platform. The selection of the PAA/GelMA matrix was based on several key considerations. PAA, a biocompatible synthetic polymer, is well known for its exceptional water absorption capacity, making it a crucial component of superabsorbent polymers for biomedical applications[36,40]. GelMA, which is known for its biocompatibility and swelling properties, effectively complements PAA. Additionally, the photocrosslinkable nature of GelMA enables the fabrication of MNs with mechanical robustness [37].

We investigated the effect of the PAA concentration on microneedle (MN) formation within a GelMA hydrogel matrix fixed at 200.0 mg/g. Three different PAA concentrations —100, 150, and 200 mg/g—were tested, with only the 100 mg/g concentration yielding MN structures. Higher PAA concentrations adversely affected the flowability and moldability of the hydrogel matrix, preventing proper filling of the molds and hindering MN formation. The PAA-GelMA hydrogel forms through physical crosslinking involving hydrogen bonding, van der Waals forces, and hydrophobic interactions [40,41]. However, this physical network lacks the mechanical integrity and stability required for MNs to penetrate the skin and effectively extract interstitial fluid (ISF) [42,43].To enhance MN properties, we introduced covalent crosslinking by UV irradiation of the PAA/GelMA matrix in the presence of a biocompatible photoinitiator (LAP) [44]. As illustrated in Figure 2A and B, the resulting MNs were seamlessly integrated into the dPAD platform, exhibiting a clear, uniform structure with a height of 1117 ± 56 μm and base width of 1044 ±73 μm. The SEM analysis (Figure 2C) further confirmed that the MNs had a smooth, non-porous surface, which contributes to maintaining structural integrity during both insertion and fluid extraction.

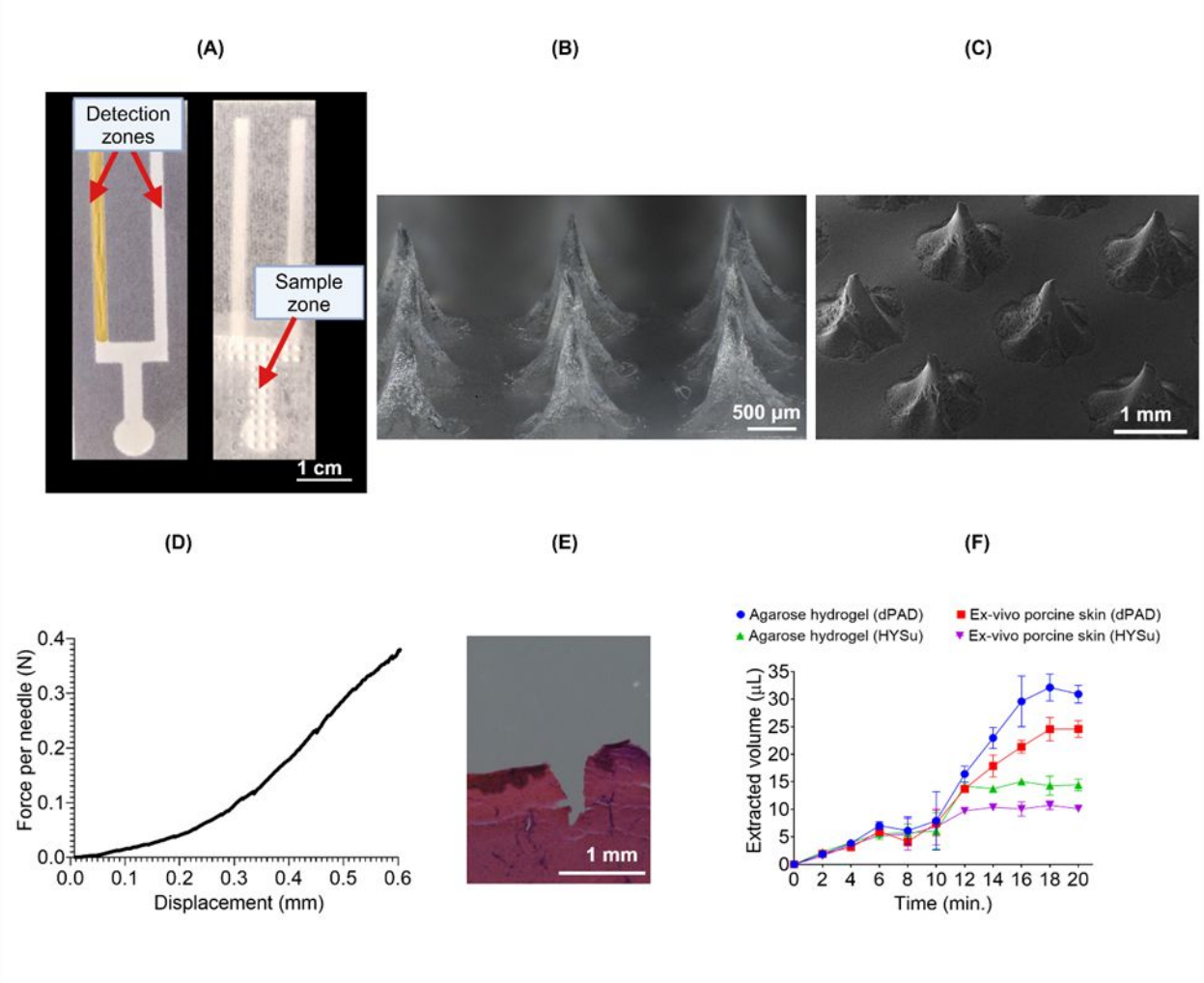

Figure 2. Characterization of dPAD Incorporated Hydrogel Microneedle Patches. (A) Fully constructed sensor patch and optical microscopic image (B) showing the hydrogel microneedle array. (C) SEM image highlighting the nonporous structure of the MNs. (D) Force-displacement curves illustrating the mechanical properties of MN patches. Data represents the average of five replicates (n = 5). (E) Skin penetration: H&E-stained section of porcine skin demonstrating penetration by the PAA/GelMA MNs array. (F) Fluid absorption: Comparison of fluid absorption kinetics in agarose hydrogel and porcine skin for MNs integrated with a hydrophobic backing layer substrate (HYSu) and those integrated within the sensor patch (dPAD).

The mechanical properties of the MN patches were assessed by measuring the force-displacement profiles under axial compression (Figure 2D). At a displacement of

450 μm, the PAA/GelMA patch withstood force of 0.25 N per needle. This value exceed the force requirements for disrupting the epidermis (0.06 N) and successful insertion without breakage (0.2 N per needle), confirming the suitability of the patch for human skin penetration[45,46]. To further evaluate skin penetration, GelMA/PAA MNs were inserted into the ex vivo porcine skin. Histological analysis of the H&E-stained skin sections (Figure 2E) revealed conical penetration cavities extending through the epidermis to a depth of approximately 790 μm, which indicates the potential of the proposed device to collect ISF while minimizing contact with the underlying nerve fibers and blood vessels [47].

As depicted in Figure 2F, when integrated onto a hydrophobic back layer, GelMA/PAA MNs achieved swelling equilibrium after 12 min., extracting 13.1 ± 0.8 μL of ISF. Embedding these MNs into a paper-based platform increased the equilibrium time to 16 min, with corresponding ISF extraction volumes of 27.3 ± 0.5 μL. To further validate the ability of GelMA/PAA MNs to extract ISF from skin, ex-vivo porcine skin was used as a model. Results demonstrated similar performance for GelMA/PAA MNs integrated onto the paper-based platform: 18 min. and 10.1 ± 0.8 μL on the hydrophobic layer, and 18 min. and 24.1 ± 0.4 μL on the paper-based platform. This extraction performance is comparable or superior to previously reported hydrogel microneedles, which generally range between 5.0 to 20.0 μL within similar or longer extraction times. For instance, Zheng et al. [48] reported an extraction volume of approximately 20.0 μL within 20 min. using swellable methacrylated hyaluronic acid-based hydrogel MNs. Similarly, Zhu et al. [37] demonstrated an ISF extraction volume of approximately 13.0 μL in 20 min. with GelMA-based MNs. These findings demonstrate that our proposed sensor patch effectively leverages the synergistic combination of hydrogel swelling and paper-based capillary action for efficient ISF extraction. Hydrophilic polymer-based hydrogel MNs swell upon skin insertion, absorbing ISF and expanding to form microchannels[22], which facilitate the transport of fluid from the dermal layers to the surface. Concurrently, the paper-based component utilizes capillary action to efficiently transport the extracted ISF, as its porous structure draws liquids through capillary forces[49]. By capitalizing on this synergistic approach, the device efficiently collected approximately 14.0 μL of ISF within 18 min. in the designated sample zone, demonstrating its potential as a wearable platform for rapid and efficient ISF collection and subsequent biomarker analysis. Since ISF

extraction did not significantly increase beyond 18 min., this duration (corresponding to swelling equilibrium) was established as the optimal extraction time for the MNs-dPAD platform.

3.2. The working principle of the developed dPAD for cortisol and dopamine detection

Distance-based paper analytical devices (dPADs) have been widely investigated across various fields, including clinical diagnostics[31,35], food safety[33], and environmental monitoring[34], due to their simplicity, cost-effectiveness, and instrument-free readout capability. In general, when a solution containing target analytes is introduced into the dPAD, the analytes immediately flow along the channel and react with the pre-deposited reagents, resulting in color changes. While the analytes react with the pre-deposited reagent, the solvent (i.e., PBS) flows to the end of the channel with the optimal sample volume. The length of the colored zone is proportional to the analyte concentration. Therefore, quantitative detection can be easily achieved by measuring the resulting color length with a traditional ruler, reducing the need for expensive instruments for signal measurement[31–33,35]. This study introduces a dPAD sensor for the simultaneous detection of cortisol and dopamine, leveraging distinct redox reactions (Figure 1C). For cortisol detection, the analyte undergoes oxidation by blue tetrazolium, followed by reduction with TMAOH, forming a nitro blue formazan compound and producing a color change from pale yellow to red-brown. Similarly, dopamine reduces Ce^{4+} to Ce^{3+}, yielding a light-brown color. To validate the feasibility of this approach, we measured the distance signals of colored products generated by varying concentrations of cortisol and dopamine. As shown in Figure 3, the resulting distance signals were 0.0, 13.3, 21.6, and 26.3 mm for cortisol at concentrations of 0.0, 4.0, 6.0, and 8.0 μg mL^{-1}, respectively, and 0.0, 12.6, 19.3, and 27.6 mm for dopamine at concentrations of 0.0, 10.0, 15.0, and 20.0 ng mL^{-1}, respectively. These results demonstrate that the proposed reactions can be effectively used for cortisol and dopamine detection through distance-based measurements, offering an instrument-free readout.

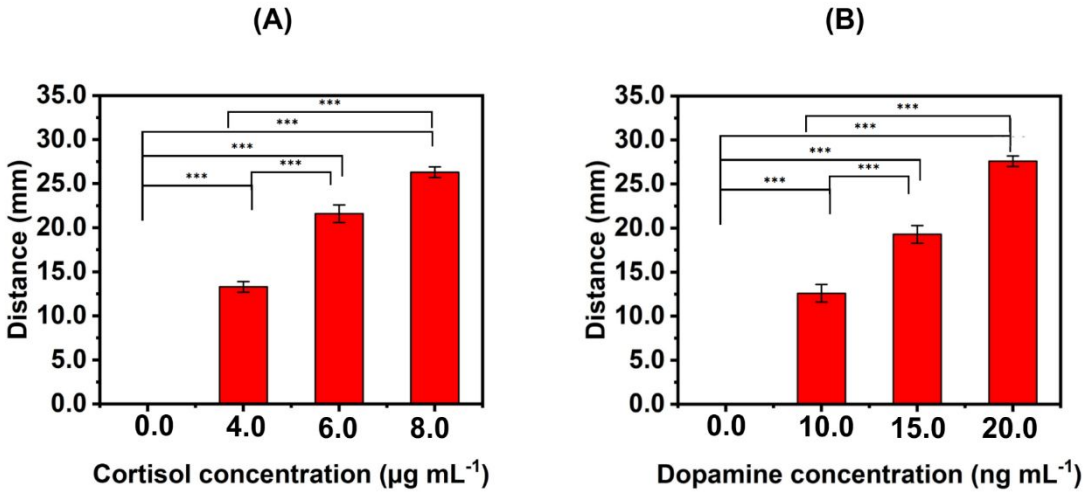

Figure 3. Analytical performance of dPAD for the detection of cortisol (A) and dopamine (B) at distinct concentrations. (***p < 0.05; one-way ANOVA with Tukey's multiple comparisons test; n = 3).

3.3. Optimization of the dPAD for cortisol and dopamine detection

We investigated key parameters influencing the performance of the proposed dPAD for detecting cortisol and dopamine. We first optimized the sample volume, as it directly correlates with the amount of target analyte available in the solution. As shown in Figure 4A, the distance signal progressively increased with increasing sample volumes from 20.0 to 30.0 µL for both biomolecules. Beyond this point, the signal plateaued up to 35.0 µL and then gradually declined due to analyte leakage from the device caused by the excess sample volume. Consequently, 30.0 µL was selected as the optimal sample volume. We confirmed that the MNs-dPAD effectively extracted ISF, obtaining approximately 14.0 µL in the sample zone within 18 min. Since our optimized analytical device requires a total sample volume of around 30 µL for optimal performance, we included an additional step in our protocol. Following ISF extraction, the MNs-dPADs were removed from the skin, and an extra 15.0 µL of phosphate-buffered saline (1× PBS) was applied directly to the sample zone. This additional step achieves the necessary total sample volume, ensuring consistent, accurate, and robust analytical detection of the target biomarkers. Furthermore, incorporating this straightforward PBS supplementation preserves the user-friendly, minimally invasive characteristics that are central to our

device's design. Next, we assessed the reaction time by tracking the signal stability after introducing a sample solution containing both cortisol and dopamine into the sample zone of the device. Figure 4B shows that the distance signals increased over time, reaching stability at 10 min, which was defined as the optimal reaction time for the device.

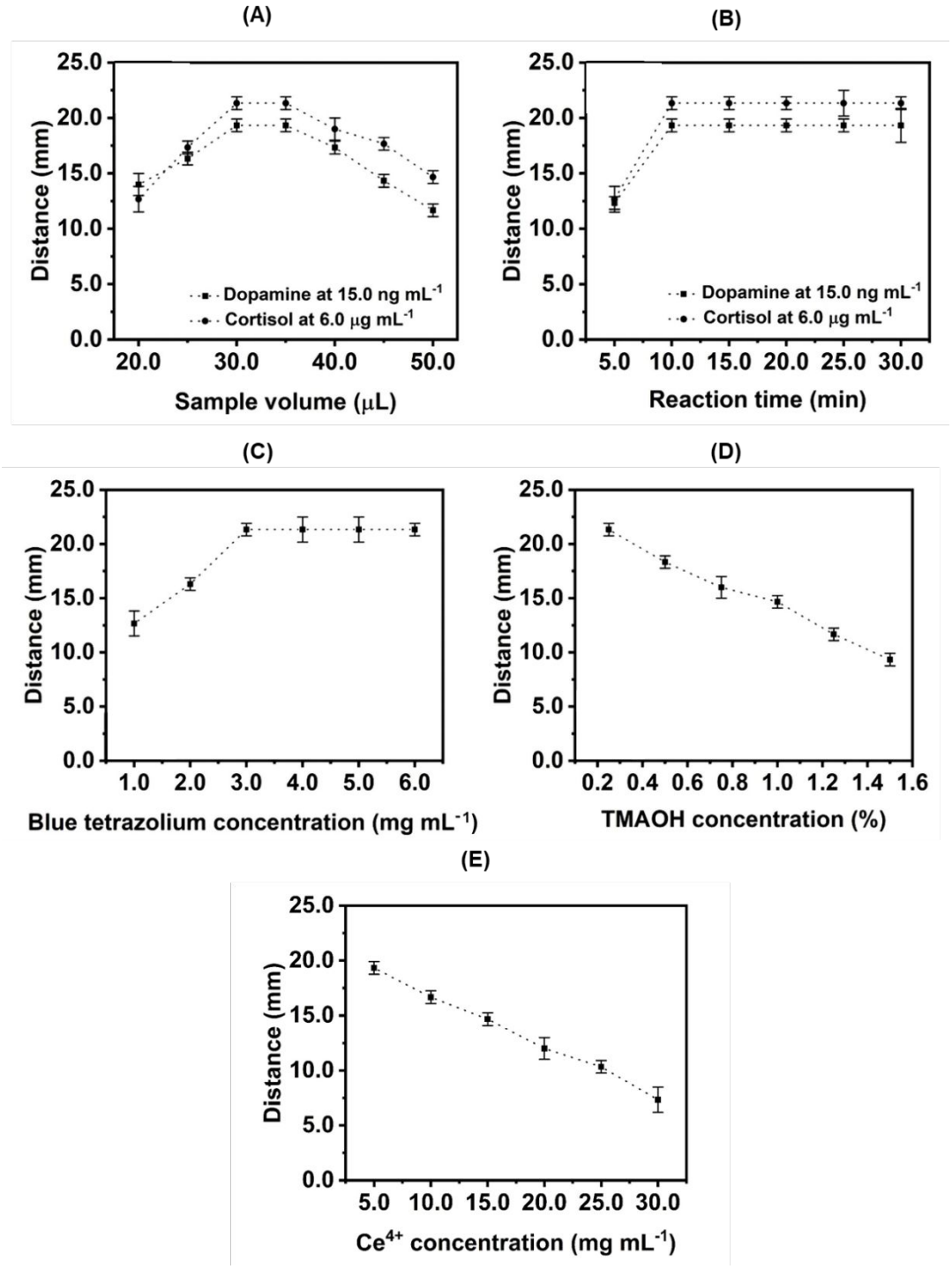

Figure 4. Optimization of the dPAD sensor parameters for cortisol and dopamine detection. (A) Distance signals as a function of sample volume for the detection of cortisol at 6.0 μg mL^{-1} and dopamine at 15.0 μg mL^{-1} (n = 3). (B) Distance signals as a function of reaction time for the detection of cortisol at 6.0 μg μg $mL^{-1}$and dopamine at 15.0 μg mL^{-1} (n = 3). (C) Distance signals as a function of blue tetrazolium concentration for the detection of cortisol at 6.0 μg mL^{-1} (n = 3). (D) Distance signals as a function of TMAOH concentration for cortisol detection at 6.0 μg mL^{-1} (n = 3). (E) Distance signals as a function of Ce^{4+} concentration for the detection of dopamine at 15.0 μg mL^{-1} (n = 3).

We further examined the concentrations of blue tetrazolium and TMAOH, as these reagents influence the formation of nitro blue formazan, which is proportional to cortisol concentration. Blue tetrazolium concentrations ranging from 1.0 to 6.0 mg mL^{-1} were tested, as shown in Figure 4C. Results indicated a significant increase in distance signals with increasing blue tetrazolium concentrations up to 3.0 mg mL^{-1}, beyond which the signals plateaued. This suggests that excess blue tetrazolium does not further react with cortisol to form additional nitro-blue formazan. Therefore, 3.0 mg mL^{-1} was selected as the optimal concentration. TMAOH concentration, evaluated between 0.25% and 1.50%, is shown in Figure 4D. Here, we observed a progressive decrease in the distance signals as the TMAOH concentration increased, likely due to the reduced binding efficiency, as described by the binding constant (Kc) in Eq. 1. Therefore, the lowest concentration (0.25 %) was selected as the optimal concentration for this approach.

$$K_c = \text{[nitro blue formazan complex]} / \text{[Cortisol-blue tetrazolium] [TMAOH]} \quad \text{(Eq. 1)}$$

Additionally, we examined Ce^{4+} concentration, which is linked to the reduction efficiency of dopamine, producing Ce^{3+} along the detection channel. Figure 4E shows that distance signals decreased gradually with increasing Ce^{4+} concentrations. Since dopamine initially reacts with Ce^{4+} to generate Ce^{3+}, an excess of Ce^{4+} causes rapid formation of Ce^{3+} until dopamine is fully consumed, making dopamine the limiting agent in the reaction. Thus, to ensure optimal detectability, the lowest Ce^{4+} concentration was chosen for this technique.

3.4. Analytical Characteristics of the dPAD sensor for cortisol and dopamine detection

We evaluated the analytical performance of the proposed dPAD sensor for simultaneous detection of cortisol and dopamine by measuring the colorimetric distance signal visible to the naked eye. Tests were conducted using a blank solution and solutions with varying biomolecule concentrations. As shown in Figure 5, the average distance signals for cortisol (2.0 μg mL^{-1}) and dopamine (5.0 ng mL^{-1}) were 7.7 mm and 7.0 mm, respectively, which were visually distinguishable from the blank signal (0.0 mm). Furthermore, the average distance signals increased proportionally with increasing cortisol and dopamine concentrations, as illustrated in Figures 5B and 5C. Linear detection ranges were established from 2.0 to 8.0 μg mL^{-1} for cortisol (R^2 = 0.9952) and from 5.0 to 25.0 ng mL^{-1} for dopamine (R^2 = 0.9943). The limits of detection (LODs) were determined based on the shortest distance signals that produced a distinguishable brown color for each analyte, enabling a reliable naked-eye readout for both cortisol and dopamine on the dPAD sensor.

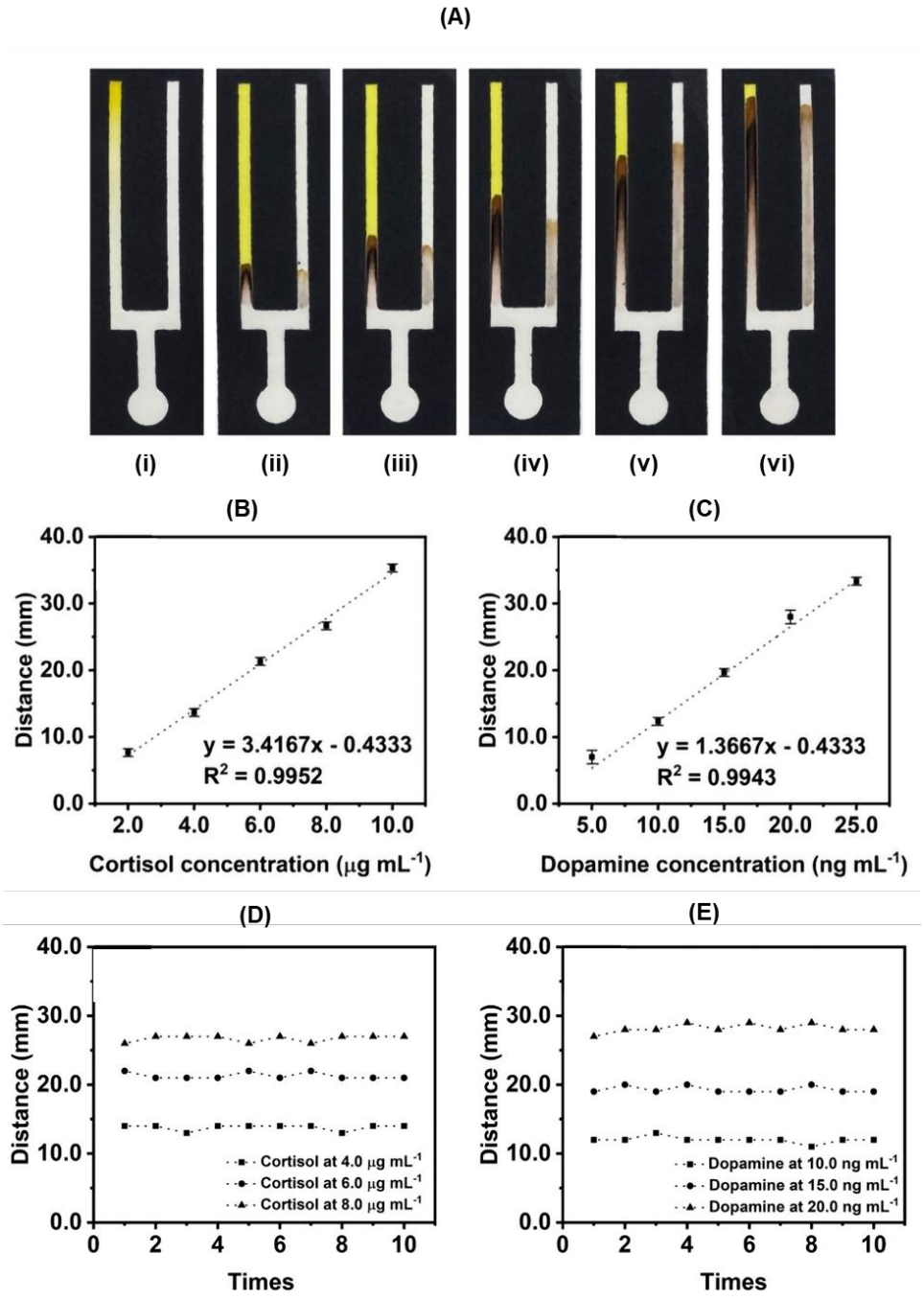

Figure 5. Performance of the dPAD sensor for simultaneous detection of cortisol and dopamine. (A) Images of the dPAD sensor for simultaneous detection of cortisol and dopamine, including (i) blank, (ii) 2.0 μg mL^{-1} and 5.0 ng mL^{-1}, (iii) 4.0 μg mL^{-1} and 10.0 ng mL^{-1}, (iv) 6.0 μg mL^{-1} and 15.0 ng mL^{-1}, (v) 8.0 μg mL^{-1} and 20.0 ng mL^{-1}, and (vi) 10.0 μg mL^{-1} and 25.0 ng mL^{-1} for cortisol and dopamine, respectively. **(B)** Linear range of cortisol detection (n = 3). **(C)** Linear range of dopamine detection (n = 3). Distance signals

demonstrating the reproducibility of the dPAD sensor in the detection of cortisol **(D)** and dopamine **(E)**.

We observed that cortisol at 0.25 μg mL⁻¹ and dopamine at 1.0 ng mL⁻¹ produced minimum detectable distance signals of 1.0 mm and 2.0 mm, respectively. To confirm these values, we measured the distance signals at these concentrations ten times (n = 10) and calculated the signal uncertainty to validate the limits of detection (LOD). The average distance signals were 1.10 mm for cortisol (0.25 μg mL⁻¹) and 1.80 mm for dopamine (1.0 ng mL⁻¹), both exceeding the three-fold standard deviations (3.S.D.) of 0.95 mm and 1.26 mm for cortisol and dopamine, respectively. Measurement uncertainty at a 99% confidence interval was calculated as 0.96 mm for cortisol and 1.27 mm for dopamine. Consequently, the uncertain distance signals for cortisol and dopamine fell within the ranges of 1.10 ± 0.95 mm and 1.80 ± 1.26 mm, respectively, lying between the blank signal (0.0 mm) and the signals for cortisol (7.7 mm at 2.0 μg mL⁻¹) and dopamine (7.0 mm at 5.0 ng mL⁻¹). Thus, we confirmed the LODs of the proposed method as 0.25 μg mL⁻¹ for cortisol and 1.0 ng mL⁻¹ for dopamine.

While data on cortisol and dopamine levels specifically in interstitial fluid (ISF) remain limited, available studies indicate that cortisol concentrations in dermal ISF typically range from approximately 0.05 μg mL^{-1} to 0.44 μg mL^{-1}, depending on circadian rhythms and individual stress levels[50–52]. Dopamine levels in ISF generally range from 0.5 to 10.0 ng mL^{-1}, influenced by various physiological and psychological states[53–55]. Our colorimetric sensor exhibits a linear detection range of 2.0–8.0 μg mL^{-1} for cortisol and 5.0–25.0 ng mL^{-1} for dopamine. Although the sensor's cortisol detection range extends beyond physiological ISF levels, its detection limit (0.25 μg mL^{-1}) aligns with the upper physiological threshold, making it relevant for monitoring elevated cortisol levels in conditions such as acute stress. For dopamine, our sensor's detection range (5.0–25.0 ng mL^{-1}) encompasses most physiologically relevant concentrations, with a detection limit (1.0 ng mL^{-1}) that further supports its practical applicability. Additionally, we assessed the precision of the device by measuring the distance signals for various biomolecule concentrations ten times (n = 10). As shown in Figures 4D and 4E, the highest relative standard deviations (RSD) were 3.06% for cortisol and 3.93% for dopamine, indicating

that our dPAD sensor offers high precision for the simultaneous quantification of both analytes.

3.5. Selectivity and study of interferents

To assess the selectivity of our dPAD sensor for cortisol and dopamine detection, we evaluated the distance signals generated by several potential interfering agents commonly present in interstitial fluid. The concentrations of the interfering substances tested in this study were selected based on their typical physiological levels in human individuals. The concentrations were intentionally chosen to exceed these normal levels to ensure a robust evaluation of our method's selectivity. By testing higher concentrations, we could better assess the sensor's capacity to distinguish cortisol and dopamine without significant interference from other substances commonly present in the interstitial fluid. Cortisol was the only analyte producing a measurable distance signal, while all other tested substances yielded signals of 0.0 mm, comparable to the blank (Figure 6A). Furthermore, no significant differences were observed between the distance signals from solutions containing only cortisol and those containing cortisol mixed with potential interferents, even at concentrations up to 5.0% (Figure 6B).

For dopamine detection, only ascorbic acid and uric acid produced slight distance signals of 1.5 mm and 1.0 mm, respectively (Figure 6C). This minor response is likely attributed to their reducing properties, which may reduce Ce^{4+} to Ce^{3+}. The limit of detection (LOD) for dopamine was determined to be 1.0 ng mL^{-1}, corresponding to a minimum distinguishable distance signal of 2.0 mm. This threshold was confirmed through repeated measurements (n = 10) with a calculated signal uncertainty of 1.27 mm at a 99% confidence interval, exceeding the baseline blank signal and statistically distinct from the lowest measured dopamine distance signal. Regarding interference, ascorbic acid and uric acid generated minor distance signals of 1.5 mm and 1.0 mm, respectively, compared to the 2.0 mm signal at the LOD. One-way ANOVA followed by Tukey’s post hoc test ($p < 0.001$) revealed statistically significant differences between the LOD signal and those produced by these potential interferents, affirming the sensor's reliability despite the minor response observed. The interference contributed less than 5% of the measured dopamine signal, as shown in Figure 6D, ensuring minimal impact on the accuracy and reliability of dopamine quantification. These findings demonstrate that our

dPAD sensor can selectively detect both cortisol and dopamine without the need for costly biorecognition elements such as antibodies or enzymes.

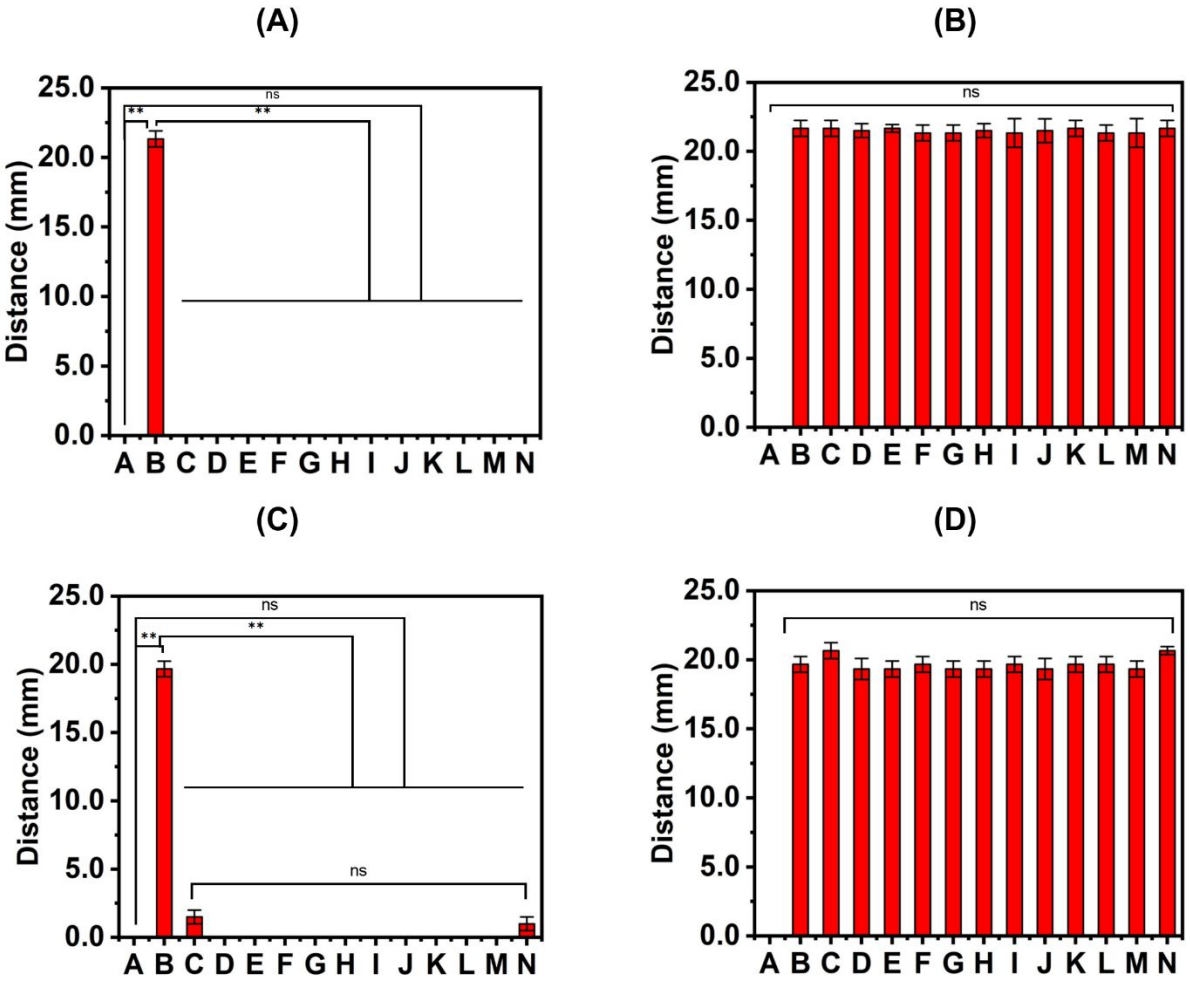

Figure 6. Selectivity and interference in cortisol and dopamine detection**. Cortisol detection:** (A) distance signals obtained for "A" a blank solution, "B" cortisol (6.0 μg mL^{-1}), and solutions of a range of potentially interfering substances including "C" ascorbic acid (10.0 mg L^{-1}), "D" BSA (100.0 g L^{-1}), "E" CRP (12.0 mg mL^{-1}), "F" creatinine (1.0 mg mL^{-1}), "G" dopamine (15.0 ng mL^{-1}), "H" fructose (50.0 mmol L^{-1}), "I" glucose (10.0 mmol L^{-1}), "J" IL-6 (120.0 ng mL^{-1}), "K" lactic acid (50.0 mmol L^{-1}), "L" TNF-α (2.0 pg mL^{-1}), "M" urea (50.0 mmol L^{-1}), and "N" uric acid (50.0 mmol L^{-1}). **(B)** Distance signal measured for "A" a blank, (B) cortisol (6.0 μg mL^{-1}), and (C-M) mixtures of cortisol (6.0 μg mL^{-1}) and the above concentrations of potentially interfering substances (n = 3). **Dopamine detection**; **(C)** distance signals obtained for "A" a blank solution, "B" dopamine (15.0 ng mL^{-1}), and

solutions of a range of potentially interfering substances including “C” ascorbic acid (10.0 mg L^{-1}), “D” BSA (100.0 g L^{-1}), “E” CRP (12.0 mg mL^{-1}), “F” creatinine (1.0 mg mL^{-1}), “G” cortisol (6.0 µg mL^{-1}), “H” fructose (50.0 mmol L^{-1}), “I” glucose (10.0 mmol L^{-1}), “J” IL-6 (120.0 ng mL^{-1}), “K” lactic acid (50.0 µmol L^{-1}), “L” TNF-α (2.0 pg mL^{-1}), “M” urea (50.0 mmol L^{-1}), and “N” uric acid (50.0 µmol L^{-1}). **(D)** Distance signals measured for “A” a blank, “B” dopamine (15.0 ng mL^{-1}), and “C-M” mixtures of dopamine (15.0 ng mL^{-1}) and above concentrations of the potentially interfering substances. (ns: not significant, $^{**}p < 0.001$; one-way ANOVA with Tukey’s multiple comparisons test; $n = 3$)

3.4. Analysis in artificial skin model

We utilized agarose hydrogel and porcine skin models saturated with artificial interstitial fluid (ISF) to evaluate the practical applications of our proposed MNs-dPAD sensor in monitoring cortisol and dopamine levels. To simulate physiological conditions, we spiked artificial ISF with varying concentrations of target biomolecules. Prior to spiking, distance signals for both cortisol and dopamine were measured at 0.0 mm, indicating the absence of these biomolecules. As the analyte concentration increased, the distance signals corresponding to the spiked artificial samples increased proportionally. As shown in Table 1, the percentage recoveries of cortisol and dopamine in the agarose hydrogel model ranged from 99.02% to 100.36% and 103.90% to 102.80%, respectively. The highest relative standard deviations (RSDs) observed were 9.12% for cortisol and 8.66% for dopamine. After successfully detecting the target analytes in the agarose hydrogel, we tested the performance of the sensor for in situ biomarker measurement using an ex vivo porcine skin model. The percentage recoveries for cortisol and dopamine in this skin model ranged from 98.29% to 103.90% and 98.29% to 104.55%, respectively (Table 2). These results demonstrate that our dPAD sensor accurately detected cortisol and dopamine in human artificial interstitial fluid, offering a simple and cost-effective solution for biomarker monitoring.

Table 1. Recovery studies for the detection of cortisol and dopamine in agarose gel (n = 3).

Biomarkers	Standard added (μg mL^{-1})	Total found (μg mL^{-1})	%Recovery	%RSD
Cortisol	0.0	0.0	-	-
	2.0	2.0	99.02	9.12
	4.0	4.2	105.61	7.14
	6.0	6.0	99.67	5.00
	8.0	8.0	100.36	3.70
Dopamine	**Standard added (ng mL^{-1})**	**Total found (ng mL^{-1})**	**%Recovery**	**%RSD**
	0.0	0.0	-	-
	5.0	5.2	103.90	8.66
	10.0	10.3	103.17	4.22
	15.0	15.7	104.55	4.76
	20.0	20.6	102.80	2.09

Table 2. Recovery studies for the detection of cortisol and dopamine in ex vivo porcine skin (n = 3).

Biomarkers	Standard added (μg mL^{-1})	Total found (μg mL^{-1})	%Recovery	%RSD
Cortisol	0.0	0.0	-	-
	2.0	2.1	103.90	8.66
	4.0	3.9	98.29	7.69
	6.0	6.2	102.93	5.59
	8.0	8.1	101.58	2.11
Dopamine	**Standard added (ng mL^{-1})**	**Total found (ng mL^{-1})**	**%Recovery**	**%RSD**
	0.0	0.0	-	-
	5.0	5.0	99.02	9.12
	10.0	9.8	98.29	7.69
	15.0	15.7	104.55	8.25
	20.0	20.1	100.36	3.70

4. Conclusions

We successfully developed the first integrated microneedle-distance-based paper analytical device (MNs-dPAD) for the simultaneous detection of cortisol and dopamine in interstitial fluid extracted from the skin, enabling the rapid, non-invasive diagnosis of chronic stress. The MNs-dPAD provides a painless and efficient method for ISF extraction, followed by on-site colorimetric detection, which is achieved via a nitro blue formazan reaction, whereas dopamine is quantified using cerium (IV) ion reduction. Visual assessment of colorimetric changes enabled quantitative analysis of both analytes within 28 min. (18 min for ISF extraction, and 10 min for sensing). Ex vivo experiments demonstrated the device's high sensitivity and specificity for clinically relevant concentrations, with a competitive limit of detection. This device is user-friendly, cost-effective, and does not require specialized equipment or training, making it ideal for POC diagnostics. While these results confirm the feasibility of ISF extraction under conditions mimicking in vivo scenarios, further validation through animal studies or clinical trials is essential to evaluate device performance comprehensively under physiological conditions. Addressing challenges such as skin elasticity, ISF volume variations, and dynamic movements will require iterative refinement of the current design. Nevertheless, the robustness and adaptability of this sensing device suggests broad potential applications in disease management and health monitoring beyond the biomarkers tested.

Author contributions

Danilo Martins dos Santos: conceptualization, methodology, investigation, validation, data curation, project administration, visualization, writing – original draft, review, and editing. **Kawin Khachornsakkul**: conceptualization, methodology, investigation, validation, data curation, project administration, visualization, writing – original draft, review, and editing. **Sameer Sonkusale**: Conceptualization, Resources, Project Administration, Writing – Review and Editing.

Conflicts of interest

The authors declare no conflicts of interest.

Acknowledgments

This work was supported by the TTW program at the Uniformed Services University of Health Sciences (USUHS) and Henry Jackson Foundation with award HU0001-20-2-0014 and HU0001-22-2-0019. S.S acknowledge the support from National Science Foundation NSF award# 1951104. Support from the DoD Peer Review Medical Research Program (award number W81XWH-21-2-0012) is also acknowledged.

References

(1) Shao, R.; Man, I. S. C.; Yau, S.-Y.; Li, C.; Li, P. Y. P.; Hou, W. K.; Li, S. X.; Liu, F. Y.; Wing, Y. K.; Lee, T. M. C. The Interplay of Acute Cortisol Response and Trait Affectivity in Associating with Stress Resilience. *Nat. Ment. Heal.* **2023**, *1* (2), 114–123. https://doi.org/10.1038/s44220-023-00016-0.

(2) Russell, G.; Lightman, S. The Human Stress Response. *Nat. Rev. Endocrinol.* **2019**, *15* (9), 525–534. https://doi.org/10.1038/s41574-019-0228-0.

(3) Baik, J.-H. Stress and the Dopaminergic Reward System. *Exp. Mol. Med.* **2020**, *52* (12), 1879–1890. https://doi.org/10.1038/s12276-020-00532-4.

(4) Lanfermeijer, M.; van Winden, L. J.; Starreveld, D. E. J.; Razab-Sekh, S.; Faassen, M. van; Bleiker, E. M. A.; van Rossum, H. H. An LC-MS/MS-Based Method for the Simultaneous Quantification of Melatonin, Cortisol and Cortisone in Saliva. *Anal. Biochem.* **2024**, *689*, 115496. https://doi.org/10.1016/j.ab.2024.115496.

(5) Akashita, G.; Nakatani, E.; Tanaka, S.; Okura, T. Development of Simultaneous Determination of Dopamine 2, Histamine 1, and Muscarinic Acetylcholine Receptor Occupancies by Antipsychotics Using Liquid Chromatography with Tandem Mass Spectrometry. *J. Pharmacol. Toxicol. Methods* **2024**, *127*, 107518. https://doi.org/https://doi.org/10.1016/j.vascn.2024.107518.

(6) Moore, T. J.; Sharma, B. Direct Surface Enhanced Raman Spectroscopic Detection of Cortisol at Physiological Concentrations. *Anal. Chem.* **2020**, *92* (2), 2052–2057. https://doi.org/10.1021/acs.analchem.9b04532.

(7) An, J. H.; Choi, D.-K.; Lee, K.-J.; Choi, J.-W. Surface-Enhanced Raman Spectroscopy Detection of Dopamine by DNA Targeting Amplification Assay in Parkisons's Model. *Biosens. Bioelectron.* **2015**, *67*, 739–746. https://doi.org/https://doi.org/10.1016/j.bios.2014.10.049.

(8) Sharma, A.; Wulff, A.; Thomas, A.; Sonkusale, S. Ultrasensitive Electrochemical Sensor for Detection of Salivary Cortisol in Stress Conditions. *Microchim. Acta* **2024**, *191* (2), 103. https://doi.org/10.1007/s00604-023-06169-0.

(9) Vignesh, V.; Castro-Dominguez, B.; James, T. D.; Gamble-Turner, J. M.; Lightman, S.; Reis, N. M. Advancements in Cortisol Detection: From Conventional

Methods to Next-Generation Technologies for Enhanced Hormone Monitoring. *ACS Sensors* **2024**, *9* (4), 1666–1681. https://doi.org/10.1021/acssensors.3c01912.

(10) Pandit, P.; Crewther, B.; Cook, C.; Punyadeera, C.; Pandey, A. K. Sensing Methods for Stress Biomarker Detection in Human Saliva: A New Frontier for Wearable Electronics and Biosensing. *Mater. Adv.* **2024**, *5* (13), 5339–5350. https://doi.org/https://doi.org/10.1039/d3ma00937h.

(11) Kelkar, N.; Prabhu, A.; Prabhu, A.; Giri Nandagopal, M. S.; Mani, N. K. Sensing of Body Fluid Hormones Using Paper-Based Analytical Devices. *Microchem. J.* **2022**, *174*, 107069. https://doi.org/10.1016/j.microc.2021.107069.

(12) Pradhan, S.; Nicholson, B. D.; Albin, S.; Heise, R. L.; Yadavalli, V. K. Single-Use Biomimetic Sensors for Rapid and Sensitive Cortisol Detection in Blood. *Biosens. Bioelectron. X* **2022**, *12*, 100280. https://doi.org/https://doi.org/10.1016/j.biosx.2022.100280.

(13) Rusheen, A. E.; Gee, T. A.; Jang, D. P.; Blaha, C. D.; Bennet, K. E.; Lee, K. H.; Heien, M. L.; Oh, Y. Evaluation of Electrochemical Methods for Tonic Dopamine Detection in Vivo. *TrAC Trends Anal. Chem.* **2020**, *132*, 116049. https://doi.org/https://doi.org/10.1016/j.trac.2020.116049.

(14) Wu, Z.; Qiao, Z.; Chen, S.; Fan, S.; Liu, Y.; Qi, J.; Lim, C. T. Interstitial Fluid-Based Wearable Biosensors for Minimally Invasive Healthcare and Biomedical Applications. *Commun. Mater.* **2024**, *5* (1), 33. https://doi.org/10.1038/s43246-024-00468-6.

(15) Parrilla, M.; Detamornrat, U.; Domínguez-Robles, J.; Donnelly, R. F.; De Wael, K. Wearable Hollow Microneedle Sensing Patches for the Transdermal Electrochemical Monitoring of Glucose. *Talanta* **2022**, *249*, 123695. https://doi.org/https://doi.org/10.1016/j.talanta.2022.123695.

(16) Poudineh, M. Microneedle Assays for Continuous Health Monitoring: Challenges and Solutions. *ACS Sensors* **2024**, *9* (2), 535–542. https://doi.org/10.1021/acssensors.3c02279.

(17) Dong, Y.; Mao, S.; Chen, S.; Ma, J.; Jaffrezic-Renault, N.; Guo, Z. Opportunities and Challenges of Microneedle Electrochemical Sensors for Interstitial Fluid Detection. *TrAC Trends Anal. Chem.* **2024**, *180*, 117891. https://doi.org/https://doi.org/10.1016/j.trac.2024.117891.

(18) Hu, Y.; Chatzilakou, E.; Pan, Z.; Traverso, G.; Yetisen, A. K. Microneedle Sensors for Point-of-Care Diagnostics. *Adv. Sci.* **2024**, *11* (12), 2306560. https://doi.org/https://doi.org/10.1002/advs.202306560.

(19) Zheng, H.; GhavamiNejad, A.; GhavamiNejad, P.; Samarikhalaj, M.; Giacca, A.; Poudineh, M. Hydrogel Microneedle-Assisted Assay Integrating Aptamer Probes and Fluorescence Detection for Reagentless Biomarker Quantification. *ACS Sensors* **2022**, *7* (8), 2387–2399. https://doi.org/10.1021/acssensors.2c01033.

(20) Dai, Y.; Nolan, J.; Madsen, E.; Fratus, M.; Lee, J.; Zhang, J.; Lim, J.; Hong, S.; Alam, M. A.; Linnes, J. C.; Lee, H.; Lee, C. H. Wearable Sensor Patch with Hydrogel Microneedles for In Situ Analysis of Interstitial Fluid. *ACS Appl. Mater. Interfaces* **2023**, *15* (49), 56760–56773. https://doi.org/10.1021/acsami.3c12740.

(21) Zheng, H.; Keyvani, F.; Sadeghzadeh, S.; Mantaila, D. F.; Rahman, F. A.; Quadrilatero, J.; Poudineh, M. Rapid MiRNA Detection in Skin Interstitial Fluid Using a Hydrogel Microneedle Patch Integrated with DNA Probes and Graphene Oxide. *Lab Chip* **2024**, *24* (21), 4989–4997. https://doi.org/10.1039/D4LC00715H.

(22) Xu, N.; Zhang, M.; Xu, W.; Ling, G.; Yu, J.; Zhang, P. Swellable PVA/PVP Hydrogel Microneedle Patches for the Extraction of Interstitial Skin Fluid toward Minimally Invasive Monitoring of Blood Glucose Level. *Analyst* **2022**, *147* (7), 1478–1491. https://doi.org/10.1039/D1AN02288A.

(23) Yao, S.; Zhang, C.; Ping, J.; Ying, Y. Recent Advances in Hydrogel Microneedle-Based Biofluid Extraction and Detection in Food and Agriculture. *Biosens. Bioelectron.* **2024**, *250*, 116066. https://doi.org/https://doi.org/10.1016/j.bios.2024.116066.

(24) Wang, Z.; Tong, S.; Niu, J.; Cao, C.; Gao, A.; Jiao, Y.; Fu, Y.; Li, D.; Pan, X.; Cui, D.; Sheng, N.; Yan, L.; Cui, S.; Lin, S.; Liu, Y. Microneedles: Multifunctional Devices for Drug Delivery, Body Fluid Extraction, and Bio-Sensing. *Nanoscale* **2025**, *17* (2), 740–773. https://doi.org/10.1039/D4NR03538K.

(25) Sliesarenko, V.; Bren, U.; Lobnik, A. Fluorescence Based Dopamine Detection. *Sensors and Actuators Reports* **2024**, *7*, 100199. https://doi.org/10.1016/j.snr.2024.100199.

(26) Zheng, L.; Zhu, D.; Xiao, Y.; Zheng, X.; Chen, P. Microneedle Coupled Epidermal Sensor for Multiplexed Electrochemical Detection of Kidney Disease Biomarkers. *Biosens. Bioelectron.* **2023**, *237*, 115506. https://doi.org/https://doi.org/10.1016/j.bios.2023.115506.

(27) Parrilla, M.; Vanhooydonck, A.; Johns, M.; Watts, R.; De Wael, K. 3D-Printed Microneedle-Based Potentiometric Sensor for PH Monitoring in Skin Interstitial Fluid. *Sensors Actuators B Chem.* **2023**, *378*, 133159. https://doi.org/https://doi.org/10.1016/j.snb.2022.133159.

(28) Zhu, D. D.; Zheng, L. W.; Duong, P. K.; Cheah, R. H.; Liu, X. Y.; Wong, J. R.; Wang, W. J.; Tien Guan, S. T.; Zheng, X. T.; Chen, P. Colorimetric Microneedle Patches for Multiplexed Transdermal Detection of Metabolites. *Biosens. Bioelectron.* **2022**, *212*, 114412. https://doi.org/https://doi.org/10.1016/j.bios.2022.114412.

(29) Wang, Z.; Li, H.; Wang, J.; Chen, Z.; Chen, G.; Wen, D.; Chan, A.; Gu, Z. Transdermal Colorimetric Patch for Hyperglycemia Sensing in Diabetic Mice. *Biomaterials* **2020**, *237*, 119782. https://doi.org/https://doi.org/10.1016/j.biomaterials.2020.119782.

(30) Hsu, W.-L.; Huang, C.-Y.; Hsu, Y.-P.; Hwang, T.-L.; Chang, S.-H.; Wang, H.-Y. J.;

Feng, L.-Y.; Tzou, S.-J.; Wei, K.-C.; Yang, H.-W. On-Skin Glucose-Biosensing and on-Demand Insulin-Zinc Hexamers Delivery Using Microneedles for Syringe-Free Diabetes Management. *Chem. Eng. J.* **2020**, *398*, 125536. https://doi.org/https://doi.org/10.1016/j.cej.2020.125536.

(31) Leelasattarathkul, T.; Trakoolwilaiwan, T.; Khachornsakkul, K. Combination of Distance-Based Paper Analytical Devices with Ionic Liquid-Based Dispersive Liquid-Liquid Microextraction for Enzyme-Free Bilirubin Quantification. *Sensors Actuators B Chem.* **2024**, *412*, 135837. https://doi.org/https://doi.org/10.1016/j.snb.2024.135837.

(32) Nguyen, M. P.; Kelly, S. P.; Wydallis, J. B.; Henry, C. S. Read-by-Eye Quantification of Aluminum (III) in Distance-Based Microfluidic Paper-Based Analytical Devices. *Anal. Chim. Acta* **2020**, *1100*, 156–162. https://doi.org/https://doi.org/10.1016/j.aca.2019.11.052.

(33) Thipwimonmas, Y.; Kongkaew, S.; Phua, C. H.; Limbut, W. A Distance-Based Paper Analytical Device: Visual Quantification of Salt in Foods with Silver Nanoparticles on Paper. *Microchem. J.* **2024**, *199*, 109853. https://doi.org/https://doi.org/10.1016/j.microc.2023.109853.

(34) Khachornsakkul, K.; Zeng, W.; Sonkusale, S. Distance-Based Paper Analytical Devices Integrated with Molecular Imprinted Polymers for Escherichia Coli Quantification. *Microchim. Acta* **2024**, *191* (5), 253. https://doi.org/10.1007/s00604-024-06332-1.

(35) Phoonsawat, K.; Khachornsakkul, K.; Ratnarathorn, N.; Henry, C. S.; Dungchai, W. Distance-Based Paper Device for a Naked-Eye Albumin-to-Alkaline Phosphatase Ratio Assay. *ACS Sensors* **2021**, *6* (8), 3047–3055. https://doi.org/10.1021/acssensors.1c01058.

(36) Dalei, G.; Das, S. Polyacrylic Acid-Based Drug Delivery Systems: A Comprehensive Review on the State-of-Art. *J. Drug Deliv. Sci. Technol.* **2022**, *78*, 103988. https://doi.org/https://doi.org/10.1016/j.jddst.2022.103988.

(37) Zhu, J.; Zhou, X.; Kim, H.-J.; Qu, M.; Jiang, X.; Lee, K.; Ren, L.; Wu, Q.; Wang, C.; Zhu, X.; Tebon, P.; Zhang, S.; Lee, J.; Ashammakhi, N.; Ahadian, S.; Dokmeci, M. R.; Gu, Z.; Sun, W.; Khademhosseini, A. Gelatin Methacryloyl Microneedle Patches for Minimally Invasive Extraction of Skin Interstitial Fluid. *Small* **2020**, *16* (16), 1905910. https://doi.org/https://doi.org/10.1002/smll.201905910.

(38) Yue, K.; Li, X.; Schrobback, K.; Sheikhi, A.; Annabi, N.; Leijten, J.; Zhang, W.; Zhang, Y. S.; Hutmacher, D. W.; Klein, T. J.; Khademhosseini, A. Structural Analysis of Photocrosslinkable Methacryloyl-Modified Protein Derivatives. *Biomaterials* **2017**, *139*, 163–171. https://doi.org/10.1016/J.BIOMATERIALS.2017.04.050.

(39) Sadeqi, A.; Kiaee, G.; Zeng, W.; Rezaei Nejad, H.; Sonkusale, S. Hard Polymeric Porous Microneedles on Stretchable Substrate for Transdermal Drug Delivery.

Sci. Rep. **2022**, *12* (1), 1853. https://doi.org/10.1038/s41598-022-05912-6.

(40) Yan, L.; Zhou, T.; Ni, R.; Jia, Z.; Jiang, Y.; Guo, T.; Wang, K.; Chen, X.; Han, L.; Lu, X. Adhesive Gelatin-Catechol Complex Reinforced Poly(Acrylic Acid) Hydrogel with Enhanced Toughness and Cell Affinity for Cartilage Regeneration. *ACS Appl. Bio Mater.* **2022**, *5* (9), 4366–4377. https://doi.org/10.1021/acsabm.2c00533.

(41) Cozens, E. J.; Roohpour, N.; Gautrot, J. E. Comparative Adhesion of Chemically and Physically Crosslinked Poly(Acrylic Acid)-Based Hydrogels to Soft Tissues. *Eur. Polym. J.* **2021**, *146*, 110250. https://doi.org/https://doi.org/10.1016/j.eurpolymj.2020.110250.

(42) Zhong, M.; Liu, Y.-T.; Liu, X.-Y.; Shi, F.-K.; Zhang, L.-Q.; Zhu, M.-F.; Xie, X.-M. Dually Cross-Linked Single Network Poly(Acrylic Acid) Hydrogels with Superior Mechanical Properties and Water Absorbency. *Soft Matter* **2016**, *12* (24), 5420–5428. https://doi.org/10.1039/C6SM00242K.

(43) Martínez, G.; Begines, B.; Pajuelo, E.; Vázquez, J.; Rodriguez-Albelo, L. M.; Cofini, D.; Torres, Y.; Alcudia, A. Versatile Biodegradable Poly(Acrylic Acid)-Based Hydrogels Infiltrated in Porous Titanium Implants to Improve the Biofunctional Performance. *Biomacromolecules* **2023**, *24* (11), 4743–4758. https://doi.org/10.1021/acs.biomac.3c00532.

(44) Xu, H.; Casillas, J.; Krishnamoorthy, S.; Xu, C. Effects of Irgacure 2959 and Lithium Phenyl-2,4,6-Trimethylbenzoylphosphinate on Cell Viability, Physical Properties, and Microstructure in 3D Bioprinting of Vascular-like Constructs. *Biomed. Mater.* **2020**, *15* (5), 55021. https://doi.org/10.1088/1748-605X/ab954e.

(45) Fonseca, D. F. S.; Vilela, C.; Silvestre, A. J. D.; Freire, C. S. R. A Compendium of Current Developments on Polysaccharide and Protein-Based Microneedles. *Int. J. Biol. Macromol.* **2019**, *136*, 704–728. https://doi.org/https://doi.org/10.1016/j.ijbiomac.2019.04.163.

(46) Davis, S. P.; Landis, B. J.; Adams, Z. H.; Allen, M. G.; Prausnitz, M. R. Insertion of Microneedles into Skin: Measurement and Prediction of Insertion Force and Needle Fracture Force. *J. Biomech.* **2004**, *37* (8), 1155–1163. https://doi.org/https://doi.org/10.1016/j.jbiomech.2003.12.010.

(47) Zhang, J.; Li, H.; Albakr, L.; Zhang, Y.; Lu, A.; Chen, W.; Shao, T.; Zhu, L.; Yuan, H.; Yang, G.; Wheate, N. J.; Kang, L.; Wu, C. Microneedle-Enabled Therapeutics Delivery and Biosensing in Clinical Trials. *J. Control. Release* **2023**, *360*, 687–704. https://doi.org/https://doi.org/10.1016/j.jconrel.2023.07.023.

(48) Zheng, M.; Wang, Z.; Chang, H.; Wang, L.; Chew, S. W. T.; Lio, D. C. S.; Cui, M.; Liu, L.; Tee, B. C. K.; Xu, C. Osmosis-Powered Hydrogel Microneedles for Microliters of Skin Interstitial Fluid Extraction within Minutes. *Adv. Healthc. Mater.* **2020**, *9* (10), 1901683. https://doi.org/https://doi.org/10.1002/adhm.201901683.

(49) Kumawat, N.; Soman, S. S.; Vijayavenkataraman, S.; Kumar, S. Rapid and Inexpensive Process to Fabricate Paper Based Microfluidic Devices Using a Cut

and Heat Plastic Lamination Process. *Lab Chip* **2022**, *22* (18), 3377–3389. https://doi.org/10.1039/D2LC00452F.

(50) Iqbal, T.; Elahi, A.; Wijns, W.; Shahzad, A. Cortisol Detection Methods for Stress Monitoring in Connected Health. *Heal. Sci. Rev.* **2023**, *6*, 100079. https://doi.org/https://doi.org/10.1016/j.hsr.2023.100079.

(51) Kaushik, A.; Vasudev, A.; Arya, S. K.; Pasha, S. K.; Bhansali, S. Recent Advances in Cortisol Sensing Technologies for Point-of-Care Application. *Biosens. Bioelectron.* **2014**, *53*, 499–512. https://doi.org/https://doi.org/10.1016/j.bios.2013.09.060.

(52) Widmer, I. E.; Puder, J. J.; König, C.; Pargger, H.; Zerkowski, H. R.; Girard, J.; Müller, B. Cortisol Response in Relation to the Severity of Stress and Illness. *J. Clin. Endocrinol. Metab.* **2005**, *90* (8), 4579–4586. https://doi.org/10.1210/jc.2005-0354.

(53) Zhao, J.; Zhao, J.; Zhang, X.; Ling, G.; Zhang, P. DNAzyme@MOF Breaking PH Limitation for the Detection of Dopamine in the Interstitial Fluid. *Biosens. Bioelectron.* **2025**, 117367. https://doi.org/https://doi.org/10.1016/j.bios.2025.117367.

(54) Liu, X.; Liu, J. Biosensors and Sensors for Dopamine Detection. *VIEW* **2021**, *2* (1), 20200102. https://doi.org/https://doi.org/10.1002/VIW.20200102.

(55) Matt, S. M.; Gaskill, P. J. Where Is Dopamine and How Do Immune Cells See It?: Dopamine-Mediated Immune Cell Function in Health and Disease. *J. Neuroimmune Pharmacol.* **2020**, *15* (1), 114–164. https://doi.org/10.1007/s11481-019-09851-4.

Data Availability Statement

The data that supports the findings of this study are available from the corresponding author upon reasonable request.